

# THE VELOCITY DISTRIBUTION OF PICKUP $\text{He}^+$ MEASURED AT 0.3 AU BY *MESSENGER*

DANIEL J. GERSHMAN<sup>1,2</sup>, LENNARD A. FISK<sup>2</sup>, GEORGE GLOECKLER<sup>2</sup>, JIM M. RAINES<sup>2</sup>,  
 JAMES A. SLAVIN<sup>2</sup>, THOMAS H. ZURBUCHEN<sup>2</sup>, AND SEAN C. SOLOMON<sup>3,4</sup>

<sup>1</sup> Geospace Physics Laboratory, NASA Goddard Space Flight Center, Greenbelt, MD 20771, USA; [djgersh@umich.edu](mailto:djgersh@umich.edu)

<sup>2</sup> Department of Atmospheric, Oceanic and Space Sciences, University of Michigan, Ann Arbor, MI 48109, USA

<sup>3</sup> Department of Terrestrial Magnetism, Carnegie Institution of Washington, Washington, DC 20015, USA

<sup>4</sup> Lamont–Doherty Earth Observatory, Columbia University, Palisades, NY 10964, USA

Received 2014 January 27; accepted 2014 March 17; published 2014 May 30

## ABSTRACT

During its interplanetary trajectory in 2007–2009, the *MERCURY Surface, Space ENvironment, GEOchemistry, and Ranging* (*MESSENGER*) spacecraft passed through the gravitational focusing cone for interstellar helium multiple times at a heliocentric distance  $R \approx 0.3$  AU. Observations of  $\text{He}^+$  interstellar pickup ions made by the Fast Imaging Plasma Spectrometer sensor on *MESSENGER* during these transits provide a glimpse into the structure of newly formed inner heliospheric pickup-ion distributions. This close to the Sun, these ions are picked up in a nearly radial interplanetary magnetic field. Compared with the near-Earth environment, pickup ions observed near 0.3 AU will not have had sufficient time to be energized substantially. Such an environment results in a nearly pristine velocity distribution function that should depend only on pickup-ion injection velocities (related to the interstellar gas), pitch-angle scattering, and cooling processes. From measured energy-per-charge spectra obtained during multiple spacecraft observational geometries, we have deduced the phase-space density of  $\text{He}^+$  as a function of magnetic pitch angle. Our measurements are most consistent with a distribution that decreases nearly monotonically with increasing pitch angle, rather than the more commonly modeled isotropic or hemispherically symmetric forms. These results imply that pitch-angle scattering of  $\text{He}^+$  may not be instantaneous, as is often assumed, and instead may reflect the velocity distribution of initially injected particles. In a slow solar wind stream, we find a parallel-scattering mean free path of  $\lambda_{\parallel} \sim 0.1$  AU and a  $\text{He}^+$  production rate of  $\sim 0.05 \text{ m}^{-3} \text{ s}^{-1}$  within 0.3 AU.

**Key words:** diffusion – ISM: atoms – methods: data analysis – scattering – solar wind – Sun: corona

**Online-only material:** color figures

## 1. INTRODUCTION

Neutral helium particles from the interstellar medium (ISM) permeate the heliosphere as the solar system moves through the local cloud at  $\sim 20 \text{ km s}^{-1}$ . Unlike neutral hydrogen, which is ionized before reaching the inner heliosphere, many helium atoms survive their heliospheric transit. These particles are not subject to strong solar radiation pressure forces, so they follow trajectories that are altered only by the Sun’s gravitational field (Figure 1). Converging trajectories of particles downwind from the direction of interstellar flow result in a region of enhanced neutral helium density commonly termed the “helium gravitational focusing cone” (Fahr 1968, 1971; Blum & Fahr 1970; Thomas 1978). During their transit, neutral helium particles can become singly charged  $\text{He}^+$  ions primarily through photoionization and, at distances less than  $\sim 0.3$  AU, by electron-impact ionization processes (McMullin et al. 2004), and become embedded in the solar wind.

Signatures of the inflow of ISM helium particles into the heliosphere have been characterized by in situ neutral particle observations (Witte et al. 1993, 2004; Bzowski et al. 2012; Möbius et al. 2012), pickup-ion measurements (Möbius et al. 1995; Möbius 1996; Noda et al. 2001; Gloeckler & Geiss 2001; Gloeckler et al. 2004; McComas et al. 2004; Saul et al. 2007; Drews et al. 2012; Gershman et al. 2013), solar wind charge-exchange emissions (Koutroumpa et al. 2009), and helium glow (Vallerga et al. 2004; Lallement et al. 2004). Whereas most in situ studies of  $\text{He}^+$  have used data at and beyond Earth’s orbit, as part of its interplanetary transfer orbit the *MERCURY Surface, Space ENvironment, GEOchemistry,*

*and Ranging* (*MESSENGER*) spacecraft (Solomon et al. 2001) traversed the helium gravitational focusing cone several times at  $\sim 0.3$  AU from 2007 to 2009 (Gershman et al. 2013). The Fast Imaging Plasma Spectrometer (FIPS) sensor (Andrews et al. 2007) on *MESSENGER* is a time-of-flight mass spectrometer capable of unambiguously identifying  $\text{He}^+$  and resolving  $\text{He}^+$  energy per charge ( $E/q$ ). Here, we conduct the first study of the velocity distributions of  $\text{He}^+$  ions that were likely injected into the solar wind in the helium gravitational focusing cone between 0.1 and 0.3 AU.

The photoionization rate of  $\text{He}^+$  scales as  $1/R^2$ , where  $R$  is heliocentric distance, enabling measurements of the extreme ultraviolet photon flux at 1 AU to be scaled to other points in the heliosphere under the assumption of isotropy. In addition, the electron-impact ionization cross-sections of helium have been well measured in the laboratory at relevant energies (Samson et al. 1994). However, the electron-impact ionization rate of interstellar neutrals depends on the local energy distribution of solar wind electrons, which has been observed to be composed of multiple components (e.g., core, halo, strahl) with differing energy and angular distributions that each vary differently with heliocentric distance and solar wind regime (Pilipp et al. 1987; Issautier et al. 1998; Maksimovic et al. 2000, 2005). Solar wind electrons have not yet been characterized in detail between 0.1 and 0.3 AU, a range of solar distances over which they are expected to be of equal if not more importance for production of  $\text{He}^+$  than photoionization (Rucinski & Fahr 1989; McMullin et al. 2004). Measurements of  $\text{He}^+$  inside 0.3 AU are extremely sensitive to the electron-impact ionization profile and are more challenging to model than those at 1 AU and beyond (Gershman

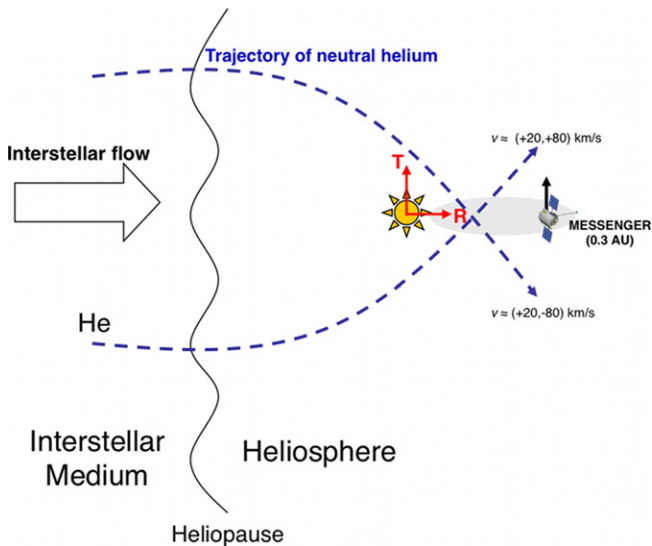


**Figure 1.** Illustration of neutral helium trajectories in the heliosphere, adapted from Gershman et al. (2013). The *MESSENGER* spacecraft transited through the helium gravitational focusing cone that forms downwind of the interstellar flow at a heliocentric distance of  $R \approx 0.3$  AU. At this distance, because of gravitational acceleration by the Sun, neutral helium particles have a non-radial velocity of  $\sim 80$  km s $^{-1}$ .

(A color version of this figure is available in the online journal.)

et al. 2013). We will therefore use parameterized neutral gas and ionization models as a guide to interpret measurements rather than attempt to fit the observations precisely.

Once ionized, helium particles are injected into the solar wind as pickup ions. These ions initially gyrate perpendicular to the embedded interplanetary magnetic field (IMF) with normalized vector  $\mathbf{w} = \mathbf{v}/v_{\text{sw}}$  defined in the solar wind rest frame, where  $\mathbf{v}$  is the velocity of the  $\text{He}^+$  ion and  $v_{\text{sw}}$  is the solar wind speed. The initial gyro-motion of a pickup ion is therefore a strong function of both the orientation of the IMF and the relative velocity between the original neutral particle and the bulk solar wind (Möbius et al. 1998, 1999). In the radial–tangential–normal ( $R$ – $T$ – $N$ ) frame of the Sun (where  $R$  is in the direction from the Sun to the point of observation,  $T$  is in the direction of the cross product of the Sun’s spin angular velocity vector and the  $R$  unit vector, and  $N$  completes the right-handed system), particles upwind from the direction of interstellar flow have sunward ( $-R$ ) velocity components of  $\sim 20$  km s $^{-1}$  with added  $-R$  velocity components due to gravitational acceleration. Particles downwind from the interstellar flow also gain a small ( $\sim 5$  km s $^{-1}$ )  $-R$  velocity component from gravitational acceleration but maintain anti-sunward ( $+R$ ) velocities of  $\sim 20$  km s $^{-1}$ . The primary effect of the Sun’s gravitational attraction is to provide a velocity component in the ( $T$ – $N$ ) plane, as illustrated in Figure 1.

The dynamics of pickup-ion evolution are dominated by two mechanisms. First, resonant interactions with magnetic fluctuations embedded in the solar wind serve to pitch-angle scatter  $\text{He}^+$  ions on a shell of constant  $|\mathbf{w}|$ . Fast pitch-angle scattering results in an increasingly isotropic distribution. Second, as these pickup-ion distributions are convected outward with the solar wind into the heliosphere, pickup-ion distributions cool, resulting in shells of smaller  $|\mathbf{w}|$ . Initially, spacecraft observations of  $\text{He}^+$  during periods of non-radial IMF (Gloeckler et al. 1995; Möbius et al. 1995) were fit with spherically symmetric distributions derived by Vasyliunas & Siscoe (1976) in the limits of fast pitch-angle scattering and adiabatic cooling.

For a radially oriented IMF, however, the measured  $\text{He}^+$  was observed to decrease (Möbius et al. 1998; Saul et al. 2004; Gloeckler et al. 2004) for  $v > v_{\text{sw}}$  relative to  $v < v_{\text{sw}}$ , indicative of strong anisotropies in the measured pickup-ion distributions. Fisk et al. (1997) interpreted a similarly observed anisotropy for  $\text{H}^+$  as resulting from a large parallel mean free path ( $\lambda_{\parallel} \sim 1$  AU). In this approximation, particle scattering is assumed to be fast for pitch angles in the ranges  $0^\circ$ – $90^\circ$  and  $90^\circ$ – $180^\circ$ , i.e., within each hemisphere, but slow across  $90^\circ$ , i.e., from one hemisphere to the other. These observations led to the development of an empirical “hemispherical” description of pickup ions in near-radial fields, formalized into models that were then used to describe spacecraft measurements of both  $\text{H}^+$  and  $\text{He}^+$  at and beyond 1 AU (Isenberg 1997; Schwadron 1998; Lu & Zank 2001).

Both parallel-propagating magnetohydrodynamic (MHD, i.e., Alfvén and fast-mode) and ion cyclotron wave modes present in the solar wind are expected to interact resonantly with  $\text{He}^+$ . MHD waves fluctuate at frequencies too low to interact resonantly with the bulk solar wind  $\text{H}^+$  ions as they propagate through the heliosphere, resulting in their ubiquitous presence in magnetic field observations (Belcher & Davis 1971; Bavassano et al. 1982; Bavassano & Smith 1986; Marsch & Tu 1990). Ion cyclotron waves, however, are able to interact resonantly with  $\text{H}^+$ , resulting in increased damping rates and ion heating (Marsch et al. 1982; Tu & Marsch 1995). Nonetheless, ion cyclotron wave modes are still observable in the solar wind and in addition can be generated locally by newly picked up ions in heliospheric, planetary, and cometary environments (Fraser 1985; Neubauer et al. 1993; Huddleston et al. 1998; Leisner et al. 2006; Jian et al. 2009). Jian et al. (2010), in particular, found evidence of discrete ion cyclotron waves propagating in the solar wind in the inner heliosphere using data from *MESSENGER*. Some of these waves were identified at 0.3 AU in the vicinity of the helium gravitational focusing cone, the same location as in our analysis here.

The inhibited pitch-angle scattering through  $90^\circ$  observed in pickup-ion measurements was explained as a “resonance gap” derived under quasi-linear theory, whereby ions with  $v \sim v_{\text{sw}}$  cannot interact with parallel-propagating transverse MHD waves (Schlickeiser 1989) or parallel-propagating ion cyclotron waves (Isenberg & Vasquez 2007) in a cold electron–proton plasma. This gap was later explicitly shown to also apply to a minor population of  $\text{He}^+$  in such a plasma by Saul et al. (2007) for the case of parallel-propagating Alfvén waves. However,  $\text{He}^+$  can, in principle, have resonant interaction with ion cyclotron waves even for  $v \sim v_{\text{sw}}$  (Isenberg & Vasquez 2007), i.e., there is no predicted resonant gap for  $\text{He}^+$  interacting with parallel-propagating ion cyclotron waves. Moreover, large-amplitude Alfvénic fluctuations observed in the solar wind are not necessarily purely transverse, with fluctuation power observed both parallel and perpendicular to the mean field (Gosling et al. 2009). Therefore, although a hemispherical distribution function description may be more appropriately applied to  $\text{H}^+$  pickup ions, it is expected that  $\text{He}^+$  particles can readily scatter through  $90^\circ$  in strong turbulence, requiring a different explanation for the measured distribution anisotropies.

Detailed in situ observations of pickup ions are challenging because of the low flux of these ions and the broad velocity distributions over large energy and angular ranges. For example, many traditional  $\text{He}^+$  measurements were accumulated over large, sunward-pointing instrument fields of view (FOVs) and then compared with a modeled analytical distribution, such as the one derived by Vasyliunas & Siscoe (1976). Although these

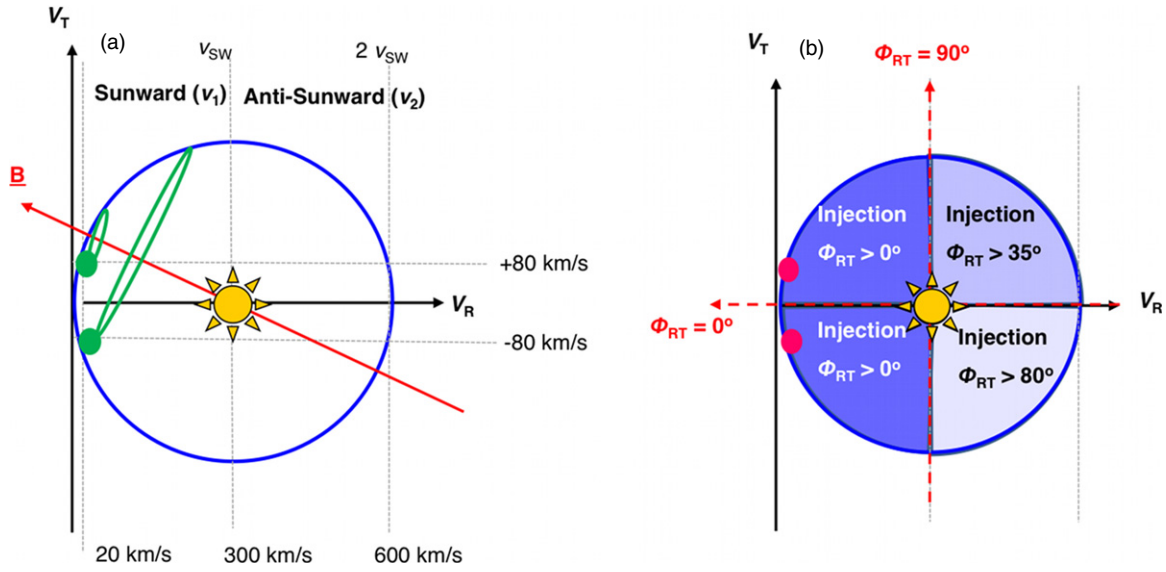


**Figure 2.** Illustration of (a) initial gyro-motion of newly ionized  $\text{He}^+$  particles at 0.3 AU in the helium focusing cone for  $v_{\text{sw}} = 300 \text{ km s}^{-1}$ , and (b) regions of initial ion gyro-motion as a function of IMF clock angle in the  $R$ - $T$  plane,  $\Phi_{\text{RT}}$ . Downwind from the interstellar flow, particles gain a variable tangential velocity component as a result of gravitational focusing by the Sun. This velocity results in a ring of initial particle injection on  $|\mathbf{w}| \sim 1$  in the solar wind frame, visible in the  $R$ - $T$  plane as two injection points. For  $\Phi_{\text{RT}} < 35^\circ$ , this gyro-motion is contained with  $V_R < v_{\text{sw}}$ . Initial gyro-motion will have  $V_R > v_{\text{sw}}$  and  $V_T < 0$  only for  $\Phi_{\text{RT}} > 80^\circ$ .

(A color version of this figure is available in the online journal.)

distributions adequately described the measured data, especially during times of non-radial IMF, the data used were not particularly sensitive to the assumptions underlying the model, and often only the  $v > v_{\text{sw}}$  hemisphere was considered. However, some three-dimensional  $\text{He}^+$  measurements have been presented from Geotail (Oka et al. 2002) and *Solar TERrestrial RELations Observatory* (Drews et al. 2013) measurements. These observations show ring and torus-like distributions of newly injected pickup ions, suggesting further that the assumption of fast pitch-angle scattering below  $90^\circ$  and slow pitch-angle scattering through  $90^\circ$  may be an oversimplification.

Consider the example of recently picked up ions at a heliocentric distance of  $R = 0.3 \text{ AU}$  in the slow solar wind ( $v_{\text{sw}} \sim 300 \text{ km s}^{-1}$ ). Here, neutral helium particles have a velocity in the  $T$ - $N$  plane of  $V_{\text{TN}} \sim 80 \text{ km s}^{-1}$ . The newly ionized  $\text{He}^+$  particles are restricted to a shell of  $|\mathbf{w}| \sim 1$  in the solar wind frame. For an IMF clock angle in the  $R$ - $T$  plane,  $\Phi_{\text{RT}}$ , of  $\sim 35^\circ$ , these constraints dictate a radial velocity of  $V_R < v_{\text{sw}}$  (Figure 2(a)). In fact, for an ecliptic Parker spiral IMF configuration, the initial gyro-motion of some ions will always take place within the  $V_R < v_{\text{sw}}$  hemisphere for both  $V_T > 0$  and  $V_T < 0$  (Figure 2(b)). When  $\Phi_{\text{TR}}$  is greater than  $35^\circ$ , some newly injected ions will be observed in the  $V_R > v_{\text{sw}}$ ,  $V_T > 0$  quadrant. Finally, injected particles will be observed in the  $V_R > v_{\text{sw}}$ ,  $V_T < 0$  quadrant only when  $\Phi_{\text{TR}} > 80^\circ$ . Therefore, for quasi-radial IMF conditions, only pitch-angle scattering through  $90^\circ$  can result in particle gyration in the  $V_R > v_{\text{sw}}$ ,  $V_T < 0$  quadrant.

Between heliocentric distances  $R_a$  and  $R_b$ , ions will cool to smaller  $|\mathbf{w}|$  shells with the mapping  $R_a/R_b = (|\mathbf{w}_a|/|\mathbf{w}_b|)^\gamma$ , where  $\gamma$  is a cooling index. Observational studies by Saul et al. (2009) and Chen et al. (2013) at 1 AU yielded values of  $\gamma$  between 1 and 2, with near-adiabatic cooling ( $\gamma = 1.5$ ) being the average behavior. In addition to cooling processes, particle energization mechanisms (Isenberg 1987; Chalov & Fahr 2000; Fisk & Gloeckler 2012) affect these distribution functions. Although these energization processes occur on longer timescales than those of adiabatic cooling, they can have a measurable effect on  $\text{He}^+$  distributions as close as 1 AU, e.g., the

formation of a suprathermal tail for  $v > 2v_{\text{sw}}$  in the instrument frame (Gloeckler et al. 2004).

In the context of pickup-ion measurements, knowledge of the cooling index,  $\gamma$ , is important for two reasons: (1) under the assumption that the mapping  $R_a/R_b = (|\mathbf{w}_a|/|\mathbf{w}_b|)^\gamma$  holds, uncertainties in  $\gamma$  correspond to uncertainties in the location of initial ion pickup; (2) this radial mapping, in concert with the distribution convection velocity, provides a timescale for distribution function evolution that can be compared with the timescales of competing processes. For  $\gamma$  between 1 and 2, pickup ions observed by FIPS at  $R = 0.3 \text{ AU}$  likely originate from  $>0.1 \text{ AU}$ , reaching 0.3 AU in less than a day. Therefore, the pitch-angle distributions of  $\text{He}^+$  measured at 0.3 AU, unlike those observed at  $>1 \text{ AU}$ , should primarily be functions of only injection, scattering, and cooling processes.

Here we use data from FIPS to derive, for the first time, the three-dimensional structure of the  $\text{He}^+$  velocity distribution inside 1 AU. These data provide an unprecedented opportunity to study the early phase of ion pickup of interstellar neutrals and enable evaluation of the commonly used spherical and hemispherical distribution function approximations. The distribution function structure will be first used to estimate the density and convection velocity of  $\text{He}^+$  as a function of heliocentric distance. These values in turn will be used to estimate the radial evolution of pickup-ion production rates inside 0.3 AU and compared with expectations from simple models. In addition, the angular structure and evolution of  $\text{He}^+$  particles in the solar wind frame will be used to investigate the interaction of  $\text{He}^+$  with magnetic turbulence, a process previously studied only at and beyond Earth's orbit. We will estimate magnetic pitch-angle scattering rates of  $\text{He}^+$  and calculate a parallel-scattering mean free path in the ecliptic at  $R = 0.3 \text{ AU}$  in the slow solar wind.

The FIPS sensor has a wide ( $\sim 1.15\pi \text{ sr}$  unobstructed) FOV, simultaneously measuring a large fraction of the  $\text{He}^+$  distribution function for a given spacecraft orientation. The *MESSENGER* spacecraft performed a number of in-flight rolling maneuvers, resulting in sampling of nearly the entire pitch-angle distribution of  $\text{He}^+$  for  $|\mathbf{w}| \sim 1$ . In Section 2, we discuss the FIPS FOV during



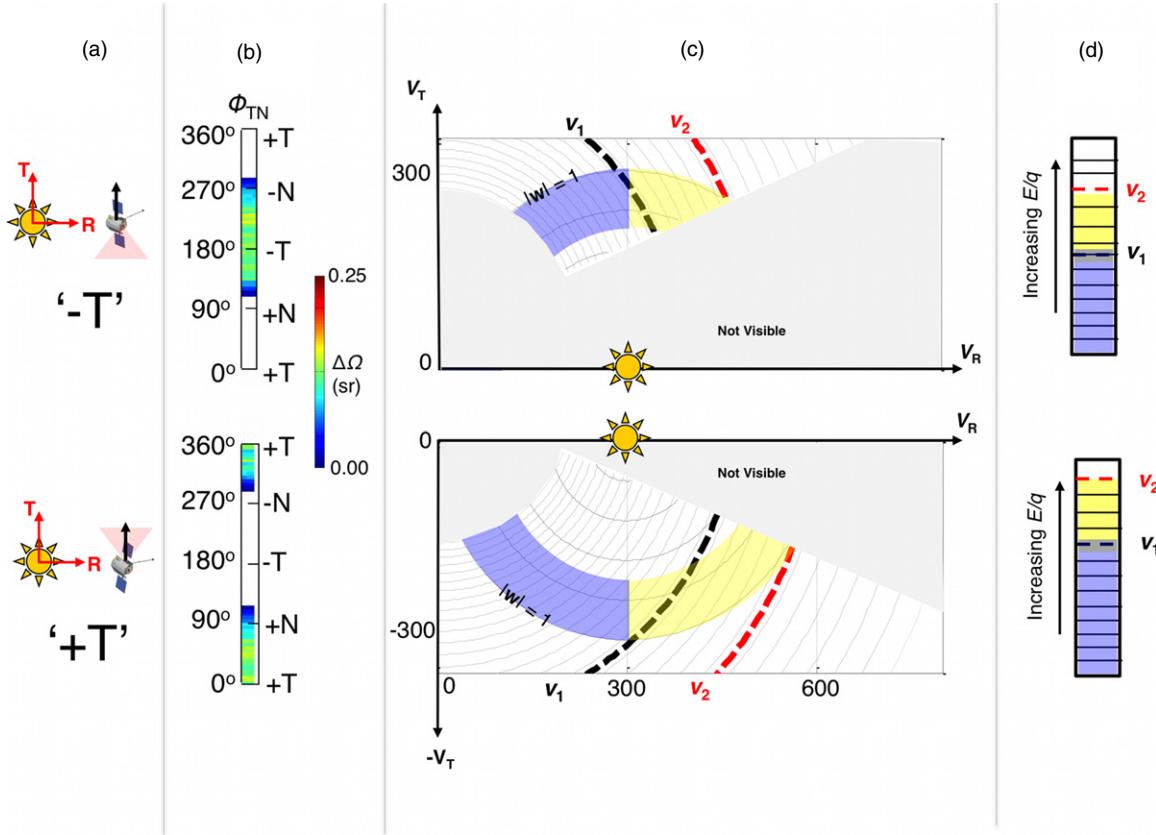


**Figure 3.** (a) Illustration of spacecraft attitude for the FIPS “ $-T$ ” (top) and “ $+T$ ” (bottom) orientations. For the  $-T$  orientation, the sensor FOV (pink triangle) is opposite that of the spacecraft velocity vector (black arrow). In the  $+T$  orientation, the sensor FOV is in the spacecraft ram direction. (b) The total visible solid angle per  $5^\circ \Phi_{TR}$  bin for each orientation. (c) The visible portion of the velocity distribution projected onto the  $R$ - $T$  plane for the “ $-T$ ” (top) and “ $+T$ ” (bottom) orientations. Spacecraft obstructions are indicated with shaded gray regions. The solar direction is obstructed by the spacecraft sunshade. Circles that originate at  $V_R \sim 0$  correspond to the FIPS energy-per-charge steps. Circles that originate at  $V_R \sim v_{sw}$  are contours of constant  $|w|$  in the solar wind frame. The black ( $v_1$ ) and red ( $v_2$ ) lines correspond to the last visible  $E/q$  step in each orientation that passes through the sunward and anti-sunward hemispheres of the  $|w| = 1$  shell, respectively. (d)  $E/q$  steps between  $v_1$  and  $v_2$  correspond to  $V_R > v_{sw}$  for  $V_T > 0$  (top) and  $V_T < 0$  (bottom). The blue and yellow shaded regions correspond to  $0.75 < |w| < 1$  in the sunward and anti-sunward hemispheres, respectively.

(A color version of this figure is available in the online journal.)

these observational time periods, and we demonstrate the effect of different spacecraft orientations on measured  $E/q$  spectra. Next, in Section 3, we introduce our data inversion procedure that enables the recovery of a pitch-angle distribution of  $\text{He}^+$  using  $E/q$  spectra at multiple spacecraft orientations without any assumption of angular structure. Although this novel technique is applied to *MESSENGER*/FIPS measurements here, it is generally applicable to other sensors with sectorized  $E/q$  observations. In Section 4, we apply this analysis to recover  $\text{He}^+$  distributions over  $0.5 < |w| < 1$ , and we discuss the implications of these observations for the heliospheric environment inside  $R = 0.3$  AU in Section 5.

## 2. FIPS OBSERVATIONS OF $\text{He}^+$ VELOCITY SPACE

Before analyzing FIPS measurements of  $\text{He}^+$ , careful consideration of both the sensor energy range and FOV must be given. During its transits through the helium focusing cone, FIPS measured  $\text{He}^+$  in 60 logarithmically spaced  $E/q$  steps between 46 eV/e and 13.6 keV/e every  $\sim 60$  s. The FIPS FOV extends out of the side of the spacecraft, with the sunward direction nominally obstructed by a spacecraft sunshade. Spacecraft rolls about the  $+R$  direction resulted in  $E/q$  sampling of  $\text{He}^+$  from a sizeable fraction of velocity space in both the sunward and anti-sunward hemispheres in the solar wind rest frame

(Gershman et al. 2013). *MESSENGER* passed through the focusing cone near the perihelion of its orbit ( $R \approx 0.3$  AU), where the spacecraft velocity was  $\sim 60$  km s $^{-1}$  in the  $+T$  direction (Figure 3(a)). This speed resulted in a non-negligible (i.e.,  $\sim 10^\circ$ ) aberration effect of measured velocities of particles with speeds comparable to that of the solar wind. This aberration enables the sensor, under favorable orientations, to measure a small fraction of the solar wind plasma, suitable for recovery of the solar wind speed (Gershman et al. 2012).

Each vector in the FIPS FOV can be projected to a clock angle in the  $T$ - $N$  plane,  $\Phi_{TN}$ . At any given time, the total solid angle projected into in all clock angles is equal to  $\sim 1.15\pi$  sr. Figure 3(b) shows the total solid angle per clock angle,  $\Phi_{TN}$ , in  $5^\circ \Phi_{TN}$  bins for two FIPS orientations denoted as “ $-T$ ” (top) and “ $+T$ ” (bottom), respectively. In the  $+T$  and  $-T$  orientations, the sensor’s FOV is centered on  $\Phi_{TR} = 90^\circ$  and  $\Phi_{TR} = 270^\circ$ , respectively, and clock angles within  $\sim 90^\circ$  of that central value can be observed. Since measured particle velocities are of the opposite sign to a sensor’s aperture direction, the  $+T$  and  $-T$  orientations measure particles with  $V_T < 0$  and  $V_T > 0$ , respectively (Figure 3(c)).  $\text{He}^+$  of solar wind origin (Gilbert et al. 2012) is excluded here by the sunshade obstruction.

Analysis of pickup  $\text{He}^+$  is often ordered in the instrument frame by energies corresponding to  $1v_{sw}$  and  $2v_{sw}$ , in particular for times of quasi-radial IMF. This ordering enables the

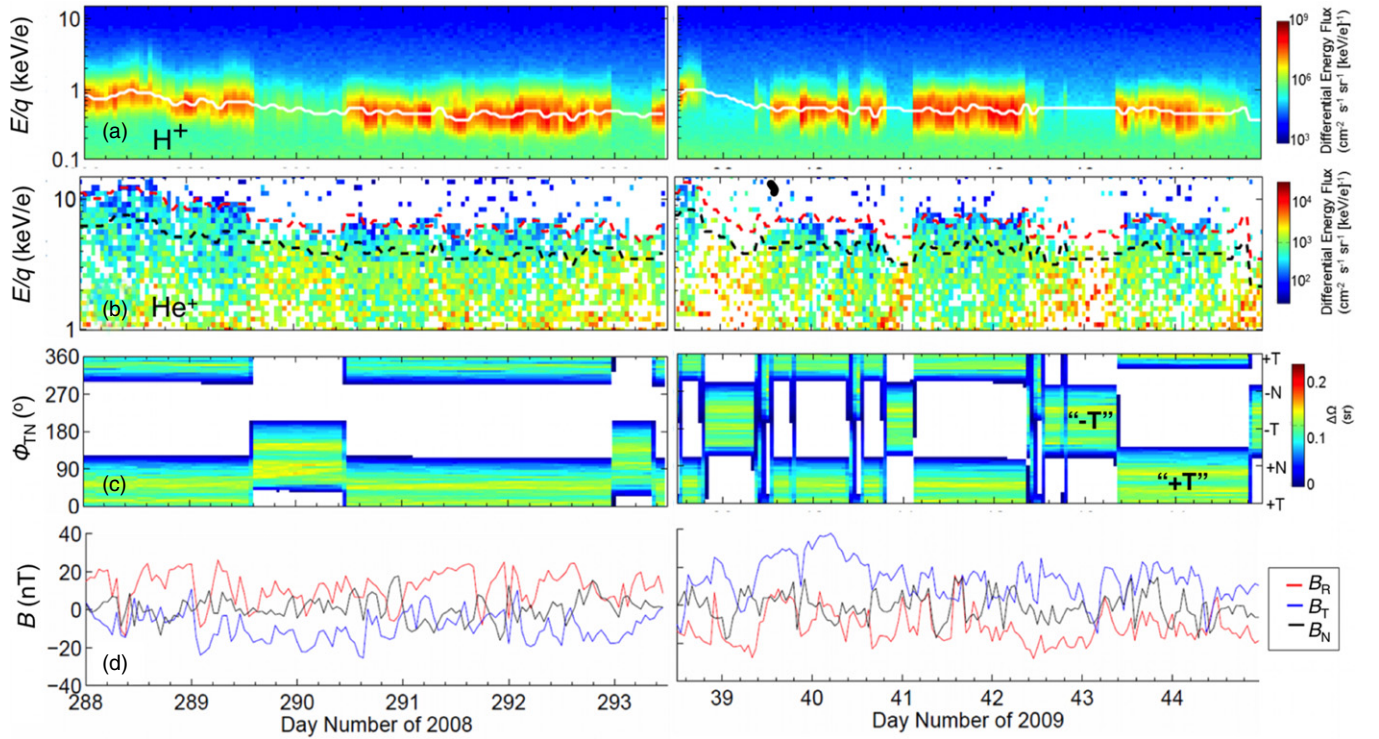


**Figure 4.** (a) H<sup>+</sup>  $E/q$  spectrogram between 0.1 and 10 keV/e for two successive transits of *MESSENGER* through the helium gravitational focusing cone in 2008 (left) and 2009 (right). The white line indicates the  $E/q$  step that corresponds to the calculated (see text) solar wind speed,  $v_{sw}$ . (b) He<sup>+</sup>  $E/q$  spectrogram between 1 keV/e and 10 keV/e. The black and red dashed lines show the  $E/q$  steps that correspond to  $v_1$  and  $v_2$ , respectively. (c) FIPS FOV solid angle projected into 5°  $\Phi_{TN}$  bins. (d) Magnetic field vectors in  $R$  (red),  $T$  (blue), and  $N$  (black) directions. All data are averaged over 1 hr.

(A color version of this figure is available in the online journal.)

distinction between the sunward and anti-sunward hemispheres with respect to the solar wind flow and examination of the cut-off of the  $E/q$  spectra. For FIPS, because of its wide FOV and obstructed sunward direction, such an analysis is not directly applicable. Instead, we define two analogous velocities, under the assumption that the pickup He<sup>+</sup> distribution is bounded by the  $|\mathbf{w}| = 1$  shell. The first,  $v_1$ , corresponds to the maximum  $E/q$  step that samples the sunward hemisphere ( $v < v_{sw}$  in the instrument frame) of the pickup-ion distribution. This value should range between  $\sim 1v_{sw}$  and  $\sim \sqrt{2}v_{sw}$ . The second,  $v_2$ , corresponds to the maximum  $E/q$  that samples the anti-sunward hemisphere ( $v > v_{sw}$  in the instrument frame) of the pickup-ion distribution. This value should range between  $\sim \sqrt{2}v_{sw}$  and  $\sim 2v_{sw}$ . Velocities  $v_1$  and  $v_2$  are indicated on Figures 3(c) and (d) with dashed black and red lines, respectively. Their precise values will depend on the instantaneous viewing geometry and solar wind velocity.

The  $E/q$  spectrograms of H<sup>+</sup> and He<sup>+</sup> averaged over 1 hr are shown for two successive *MESSENGER* cone transits in 2008 and 2009 in Figures 4(a) and (b), respectively. The average angular distance of *MESSENGER* from the cone center during these transits was  $\sim 15^\circ$ . A white line appears on the H<sup>+</sup> flux showing the computed solar wind energy in Figure 4(a). H<sup>+</sup> flux increases are observed when the spacecraft is oriented in the + $T$  direction (illustrated in Figure 3(c)) due to solar wind aberration effects. When there were not sufficient H<sup>+</sup> events to recover an estimated solar wind speed, a linearly interpolated value was used. He<sup>+</sup> events are background corrected, and only  $E/q$  steps above 1 keV/e are shown. Magnetic field vectors from the Magnetometer (Anderson et al. 2007) instrument on *MESSENGER* are also included and are averaged over 1 hr (Figure 4(d)).

As discussed by Gershman et al. (2013), the measured He<sup>+</sup> flux is a function of both solar wind speed and spacecraft orientation. When the He<sup>+</sup> distribution is within the sensor's  $E/q$  range, i.e.,  $v_{sw} \lesssim 450 \text{ km s}^{-1}$  ( $E/q \lesssim 1 \text{ keV}$ ), the  $v_2$  line (red in Figure 4(b)) forms a bound for the measured He<sup>+</sup> flux. Such an outcome suggests that the He<sup>+</sup> is well bounded by the  $|\mathbf{w}| = 1$  shell, indicating that no substantial energization of He<sup>+</sup> has occurred. There is, however, substantial flux between the  $v_1$  and  $v_2$  lines for the + $T$  orientation for all observable solar wind speeds and quasi-radial IMF. These fluxes correspond to the  $V_R > v_{sw}$ ,  $V_T < 0$  quadrant, where particles cannot easily be directly injected, unambiguously indicating that there has been substantial pitch-angle scattering across  $90^\circ$  during these time periods. The changes in measured flux with orientation observed in Figure 4 will be both a function of the He<sup>+</sup> phase-space density and the fraction of the distribution sampled by the sensor. These effects must be decoupled before developing additional conclusions about the measured He<sup>+</sup> fluxes pertaining to scattering rates, densities, or mean free paths.

### 3. PITCH-ANGLE DISTRIBUTIONS FROM $E/q$ MEASUREMENTS

To derive the pitch-angle distribution of He<sup>+</sup>, we must first convert measured events into phase-space density. The number of events observed by FIPS in an  $E/q$  scan,  $N(v)$ , can be converted to physical units through scaling by the instrument geometric factor ( $g_{eff}$ ), sensor efficiency ( $\eta$ ), and observation time ( $\Delta t$ ) (Raines et al. 2011), to form the function  $f(v)$  with units  $\text{s}^3 \text{ m}^{-6} \text{ sr}$ , i.e.,

$$f(v) \equiv \frac{N(v)}{v_{FIPS}^4 g_{eff} \eta \Delta t}. \quad (1)$$

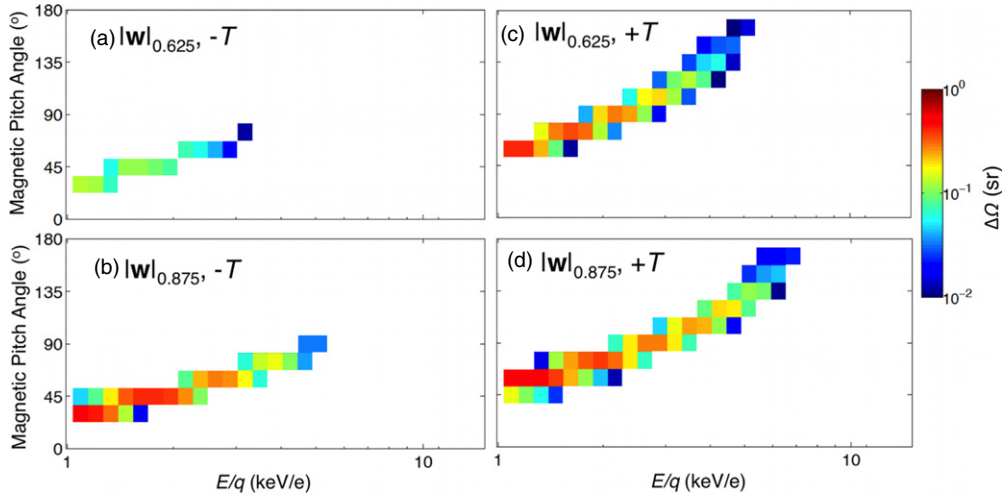


**Figure 5.**  $\Delta\Omega(|\mathbf{w}|, \mu, v)$  for  $|\mathbf{w}|_{0.625}$  and  $|\mathbf{w}|_{0.875}$  shells for the ((a) and (b))  $-T$  and ((c) and (d))  $+T$  orientations. Each pixel corresponds to a  $15^\circ$  magnetic pitch-angle bin and a single FIPS  $E/q$  step. For the  $-T$  orientation, the visibility of the  $|\mathbf{w}|_{0.875}$  shell is much greater than that of the  $|\mathbf{w}|_{0.625}$  shell for all  $E/q$  steps. For the  $+T$  orientation, the visibility of the  $|\mathbf{w}|_{0.875}$  shell is at least twice that of the  $|\mathbf{w}|_{0.625}$  shell for  $E/q$  values  $> 3.75$  keV/e.

(A color version of this figure is available in the online journal.)

In Equation (1),  $f(v)$  is implicitly integrated over the portion of the three-dimensional sampled distribution  $f(v, \theta, \varphi)$ , that falls within the FIPS FOV, where  $\theta$  and  $\varphi$  are the polar and azimuthal angles in spherical coordinates, respectively,

$$f(v) \equiv \int_{\text{FOV}} f(v, \theta, \varphi) d\Omega. \quad (2)$$

The units of  $f(v, \theta, \varphi)$  are that of phase-space density, i.e.,  $\text{s}^3 \text{m}^{-6}$ . For a gyro-tropic pitch-angle distribution in the solar wind frame,  $f(v, \theta, \varphi) = f(|\mathbf{w}|, \mu)$ , where  $\mu$  is the cosine of the magnetic pitch angle. Here, each distribution “shell” is defined by its  $|\mathbf{w}|$  value. These shells, in general, do not define surfaces of constant phase-space density and instead may exhibit structure with  $\mu$ .

The integral in Equation (2) can be approximated by a sum of a finite number of  $|\mathbf{w}|$  and  $\mu$  bins and rewritten as

$$f(v) = \sum_{|\mathbf{w}|, \mu} f(|\mathbf{w}|, \mu) \Delta\Omega(|\mathbf{w}|, \mu, v). \quad (3)$$

For a particular orientation of FIPS, the  $\Delta\Omega$  coefficients in Equation (3) can be determined by mapping the three-dimensional sensor FOV ( $v, \theta, \varphi$ ) bins into the appropriate set of  $(|\mathbf{w}|, \mu, v)$  bins. Here, we use two  $|\mathbf{w}|$ -shell bins:  $|\mathbf{w}|_{0.625}$  corresponds to  $0.5 < |\mathbf{w}| < 0.75$ , and  $|\mathbf{w}|_{0.875}$  corresponds to  $0.75 < |\mathbf{w}| < 1$ . An example of the  $\Delta\Omega$  coefficients for each of these shells in the FIPS FOV is shown in Figure 5 for a solar wind velocity of  $300 \text{ km s}^{-1}$ , a Parker-spiral angle of  $\Phi_{\text{TR}} = -25^\circ$ , and a  $15^\circ$  angular resolution for the  $+T$  and  $-T$  orientations. Bins with  $\Delta\Omega < 0.01$  sr are excluded. For the  $-T$  orientations, the visible solid angle of the  $|\mathbf{w}|_{0.875}$  shell (Figure 5(d)) is at least twice that of the  $|\mathbf{w}|_{0.625}$  shell (Figure 5(c)) for all  $E/q$  steps  $> 1$  keV/e. For the  $+T$  orientation, the visible solid angle of the  $|\mathbf{w}|_{0.875}$  shell (Figure 5(b)) is at least twice that of the  $|\mathbf{w}|_{0.625}$  shell (Figure 5(a)) for  $E/q > 3.75$  keV/e. The values of these coefficients are also listed in Tables 1–4 in the Appendix. As will be shown in the subsequent sections, a known set of  $\Delta\Omega$  coefficients and measured  $f(v)$  values can result in estimates of  $f(|\mathbf{w}|, \mu)$ , which in turn can be used to estimate helium production and scattering rates inside 0.3 AU.

### 3.1. Direct Recovery of $f(|\mathbf{w}|, \mu)$

Applying Equation (3) to multiple  $E/q$  steps results in a set of first-order linear equations of the form  $A\mathbf{x} = \mathbf{B}$ , where  $A$  is a matrix of the  $\Delta\Omega$  coefficients,  $\mathbf{B}$  contains the instrument-measured  $f(v)$  values, and  $\mathbf{x}$  is the pitch-angle distribution function  $f(|\mathbf{w}|, \mu)$  computed at discrete values. Standard linear regression techniques can be applied to this system to minimize the norm of the residual  $\|(\sum_{|\mathbf{w}|, \mu} f(|\mathbf{w}|, \mu) \Delta\Omega(|\mathbf{w}|, \mu, v)) / f(v) - 1\|^2$  subject to the constraint  $f(|\mathbf{w}|, \mu) \geq 0$ . Here, each quantity in  $\sum_{|\mathbf{w}|, \mu} f(|\mathbf{w}|, \mu) \Delta\Omega(|\mathbf{w}|, \mu, v)$  is normalized by its corresponding measured  $f(v)$  value. This normalization weights each point in the regression equally rather than favoring those with higher values of  $f(v)$ . The recovered  $f(|\mathbf{w}|, \mu)$  function will be limited by the solid angle coverage of each  $(|\mathbf{w}|, \mu, v)$  bin.

The choice of angular structure here is arbitrary, though the use of too few bins will result in overestimation and underestimation of the distribution in places, and the use of too many bins will result in an underdetermined solution. Given the spacing of the  $E/q$  steps of FIPS, the maximum angular resolution used is  $15^\circ$ . There are  $(|\mathbf{w}|, \mu, v)$  bins that are poorly observed that will create uncertainties in the recovered  $f(|\mathbf{w}|, \mu)$  distribution. To quantify these uncertainties, we calculate the amount by which each point in the  $f(|\mathbf{w}|, \mu)$  solution can be increased or decreased before the regression residual increases 5% over its minimum value. Those points that have recovered values that are exactly zero are excluded from the reported solution.

### 3.2. Calculation of $\text{He}^+$ Plasma Parameters

By taking moments of a pitch-angle distribution  $f(|\mathbf{w}|, \mu)$ , we can estimate the partial density ( $n_{\text{He}^+}$ ) and effective convection velocity ( $v_{\text{He}^+}$ ) of  $\text{He}^+$  per shell. The total pickup-ion density will be the amalgamation of the densities of all ions in all shells. However, here we examine each of the measured shells individually, as they map to different regions of space in the inner heliosphere. The partial density in a given shell will correspond to the total ion content picked up at a given heliocentric distance. We also assume that a given pitch-angle distribution is confined to a thin (mean energy  $|\mathbf{w}|$  and width  $\Delta|\mathbf{w}| = |\mathbf{w}|$ ) gyro-tropic



shell, resulting in

$$n_{\text{He}^+} = v_{\text{sw}}^3 \left( 2\pi |\mathbf{w}|^2 \Delta |\mathbf{w}| \int_{-1}^1 f(|\mathbf{w}|, \mu) d\mu \right), \quad (4)$$

and

$$v_{\text{He}^+} = v_{\text{sw}} \left( 1 - \frac{\int_{-1}^1 \mu f(|\mathbf{w}|, \mu) d\mu}{\int_{-1}^1 f(|\mathbf{w}|, \mu) d\mu} |\mathbf{w}| |\hat{\mathbf{R}} \cdot \hat{\mathbf{B}}| \right). \quad (5)$$

The partial density in a  $|\mathbf{w}|$  shell should not be affected by pitch-angle scattering processes. Therefore the  $n_{\text{He}^+}$  calculated from observed distributions can be used to scale the partial density of any modeled distribution of particle injection. Convection velocity,  $v_{\text{He}^+}$ , however, will be a strong function of pitch-angle scattering. An isotropic distribution will yield  $v_{\text{He}^+} = v_{\text{sw}}$ . For distributions with a sunward anisotropy,  $v_{\text{He}^+}$  will be less than  $v_{\text{sw}}$ .

The entire pitch-angle distribution for a given shell is not necessarily visible, which can lead to biases in the calculation of  $n_{\text{He}^+}$  and  $v_{\text{He}^+}$ . To account for this bias,  $n_{\text{He}^+}$  and  $v_{\text{He}^+}$  are calculated in two ways. First, the plasma parameters are calculated using only the data available and setting  $f(|\mathbf{w}|, \mu) = 0$  in all unobserved areas. Second, we calculate the plasma parameters using linear interpolation and nearest neighbor extrapolation to ensure that all  $f(|\mathbf{w}|, \mu) > 0$ . These two sets of parameters are considered to be the range of uncertainty for the computed moments. This definition of uncertainty invokes the implicit assumption that the phase-space density at unobserved pitch angles is not significantly larger than that at the observed pitch angles. Nevertheless, observation of a large fraction of pitch angles in a given shell, in particular for one in which the phase-space density has evolved in time due to scattering, should lead to representative estimates of  $n_{\text{He}^+}$  and  $v_{\text{He}^+}$ .

#### 4. He<sup>+</sup> DISTRIBUTION FUNCTIONS AT $R = 0.3$ AU

In order to apply the recovery of  $f(|\mathbf{w}|, \mu)$  described in Section 3, the transformation between the instrument frame and solar wind frame must be well known. This transformation is sensitive to the sensor FOV, the solar wind speed, and the average orientation of the IMF. Here, we take data only from  $E/q$  scans by FIPS during the 2009 cone transit during which the solar wind speed was between 275 and 325 km s<sup>-1</sup>, and the IMF averaged over the scan time was within 30° of the Parker spiral direction expected for 300 km s<sup>-1</sup> solar wind at 0.3 AU, i.e.,  $\Phi_{\text{TR}} = -25^\circ$ . Data from the  $+T$  and  $-T$  orientations were accumulated together to form orientation-averaged  $f(v)$  distributions. These values are listed in Table 5 in the Appendix.

##### 4.1. Initial Ion Injection

Here we are interested in the angular structure of  $f(|\mathbf{w}|, \mu)$ . Therefore, to provide a baseline comparison for our measurements, we model the initial pitch-angle distribution of newly injected pickup ions. With cooling indices between  $\gamma = 1$  and  $\gamma = 2$ , the  $|\mathbf{w}|_{0.625}$  and  $|\mathbf{w}|_{0.875}$  shells map to mean heliocentric distances of  $\sim 0.15$  AU and  $\sim 0.25$ , respectively. At those distances for 300 km s<sup>-1</sup> solar wind in the ecliptic, we expect  $\Phi_{\text{TR}} \sim 12^\circ$  and  $\Phi_{\text{TR}} \sim 20^\circ$  and non-radial neutral helium velocities of  $\sim 110$  km s<sup>-1</sup> and  $\sim 85$  km s<sup>-1</sup>, respectively. For each heliocentric distance, we calculate the pitch-angle distribution of a number of test particles under a randomized solar wind speed between 275 and 325 km s<sup>-1</sup> and a randomized angle

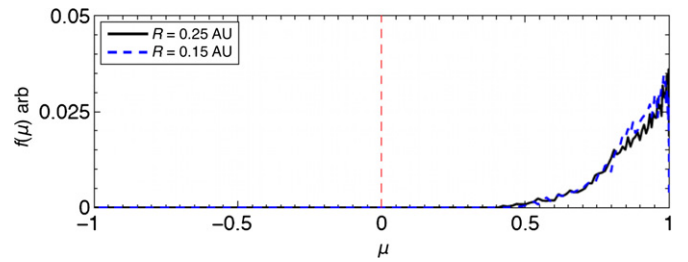


**Figure 6.** Modeled injected  $f(\mu)$  distributions for particles injected at 0.15 AU ( $|\mathbf{w}|_{0.625}$  shell at 0.3 AU) and at 0.25 AU ( $|\mathbf{w}|_{0.875}$  shell at 0.3 AU). Due to an average near-radial IMF at these distances, initial ion gyro-motion peaks at magnetic pitch angles near  $0^\circ$ . Varying solar wind conditions and IMF orientations lead to a spread in the distribution.

(A color version of this figure is available in the online journal.)

within a cone of  $30^\circ$  of the  $\Phi_{\text{TR}}$  direction. The neutral velocities at both distances result in initial pickup on  $|\mathbf{w}| \sim 1$ .

Varying solar wind conditions and non-radial neutral injection velocities create a  $f(\mu)$  distribution that is not simply a ring, but rather a torus-like distribution with a sharp peak, as shown in Figure 6. We can estimate the convection velocity of injected particles using these distributions and Equation (5). For  $|\mathbf{w}| = 1$ ,  $\Delta|\mathbf{w}| = 0.01$ ,  $v_{\text{sw}} = 300$  km s<sup>-1</sup>, and  $\Phi_{\text{TR}}$ , we find initial convection velocities of  $v_{\text{He}^+} \sim 45$  and  $\sim 60$  km s<sup>-1</sup> for particles injected at 0.15 and 0.25 AU, respectively. We expect that the distributions observed by FIPS should correspond to time- and space-evolved states of these initially injected distributions.

##### 4.2. Recovered Distributions

As discussed in Section 3, the  $|\mathbf{w}|_{0.875}$  shell is better observed by FIPS for both the  $+T$  and  $-T$  sensor orientations. Therefore, we can decompose our calculation of  $f(|\mathbf{w}|, \mu)$  into two separate linear regression problems. Each regression will be used to solve only for the angular structure in a single  $|\mathbf{w}|$  shell, reducing the total number of free parameters for a given inversion. First, we solve for  $f(|\mathbf{w}|_{0.825}, \mu)$  using  $E/q$  steps that have at least twice the solid angle coverage of the  $|\mathbf{w}|_{0.875}$  shell than of the  $|\mathbf{w}|_{0.625}$  shell. Second, we use the remaining  $E/q$  steps and the newly recovered  $f(|\mathbf{w}|_{0.875}, \mu)$  distribution to calculate  $f(|\mathbf{w}|_{0.625}, \mu)$ . Restricting our analysis to  $E/q$  steps most sensitive to the  $|\mathbf{w}|_{0.875}$  shell simplifies Equation (3) to yield

$$f_{-T}(v) \approx \sum_{\mu} f(|\mathbf{w}|_{0.875}, \mu) \Delta\Omega_{-T}(|\mathbf{w}|_{0.875}, \mu, v), \quad (6)$$

and

$$f_{+T} \left( \frac{E}{q} > 3.5 \text{ keV/e} \right) \approx \sum_{\mu} f(|\mathbf{w}|_{0.875}, \mu) \Delta\Omega_{+T}(|\mathbf{w}|_{0.875}, \mu, v). \quad (7)$$

Here, the subscripts  $+T$  and  $-T$  denote the geometric orientation of the measurement previously defined. For the remaining  $E/q$  steps in the  $+T$  orientation,

$$f_{+T} \left( \frac{E}{q} < 3.5 \text{ keV/e} \right) \approx \sum_{\mu} f(|\mathbf{w}|_{0.625}, \mu) \Delta\Omega_{+T}(|\mathbf{w}|_{0.625}, \mu, v) + \sum_{\mu} f(|\mathbf{w}|_{0.875}, \mu) \Delta\Omega_{+T}(|\mathbf{w}|_{0.875}, \mu, v). \quad (8)$$

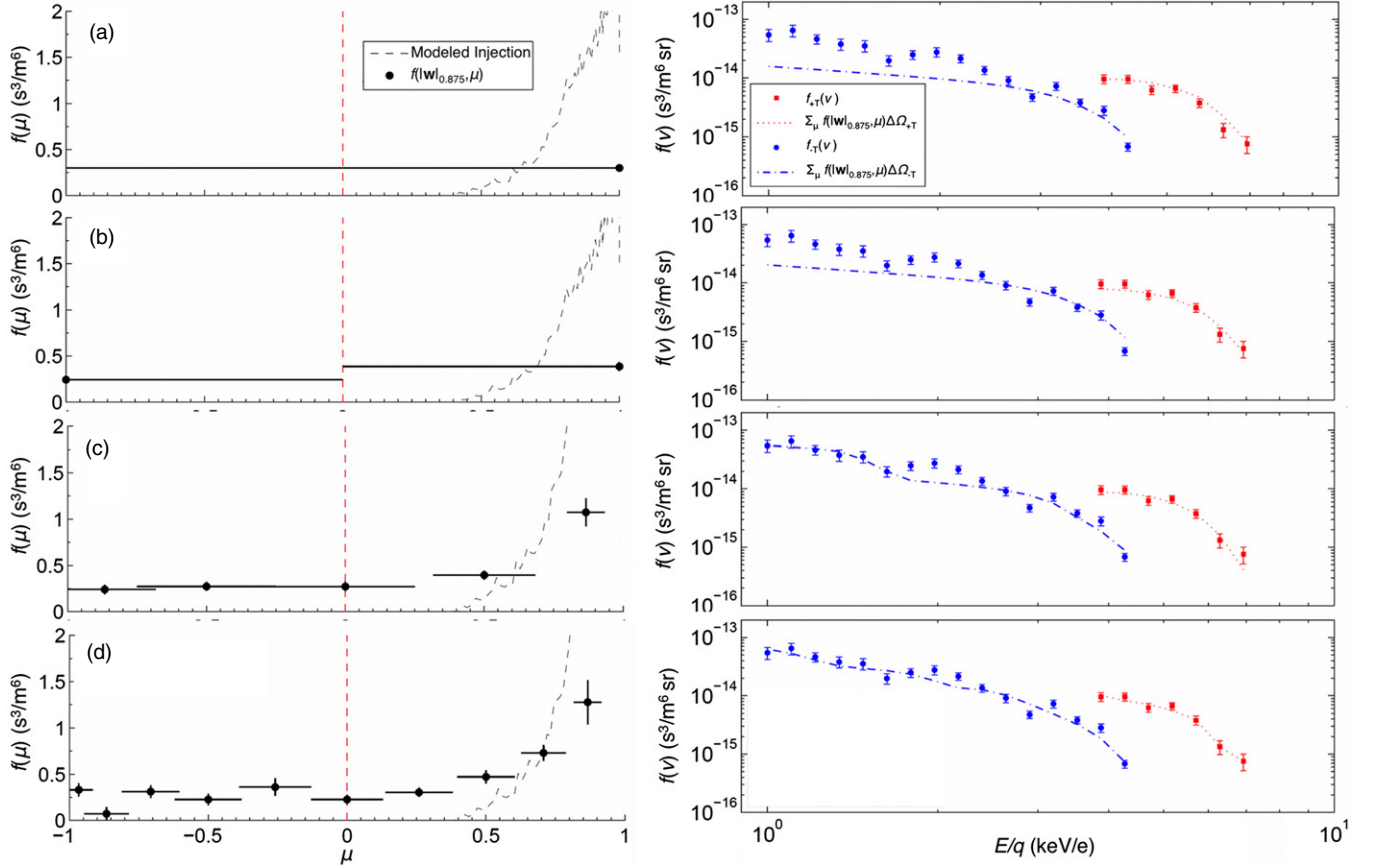


**Figure 7.** Left: recovered phase-space density as a function of magnetic pitch angle for the  $|\mathbf{w}|_{0.875}$  shell for (a) an isotropic solution, (b) a hemispherical solution, (c) a solution with  $30^\circ$  angular resolution, and (d) a solution with  $15^\circ$  angular resolution. The recovered distributions are those that minimize the residual  $\|(\sum_{\mu} f(|\mathbf{w}|, \mu) \Delta\Omega(|\mathbf{w}|, \mu, v))/f(v) - 1\|^2$ . The horizontal bars represent the angular extent of each bin, and the vertical bars represent the recovery uncertainties, as described in Section 3.1. Angular bins that do not contribute to the solution are not shown. The modeled injection distribution is shown as a black dashed line. Right: a solution that monotonically decreases with pitch angle is required to best-match  $f_{+T}(v)$  and  $f_{-T}(v)$ , shown as red squares and blue circles, respectively. The uncertainties shown are counting statistics; the  $1/\sqrt{N}$  value at each point is used as the relative error. The red dashed and blue dash-dotted lines are the corresponding  $\sum_{\mu} f(|\mathbf{w}|_{0.825}, \mu) \Delta\Omega(|\mathbf{w}|_{0.825}, \mu, v)$  values for each  $E/q$  step and are subtracted from the measured  $f(v)$  values to calculate the regression residual. (A color version of this figure is available in the online journal.)

#### 4.2.1. Recovery of the $|\mathbf{w}|_{0.875}$ Shell

For the  $|\mathbf{w}|_{0.875}$  shell we examine an isotropic solution ( $1 \mu$  bin), a hemispherical solution ( $2 \mu$  bins), a  $30^\circ$  solution ( $6 \mu$  bins), and a  $15^\circ$  solution ( $12 \mu$  bins), as shown in Figure 7. For all of the solutions, the modeled distribution is scaled so that its total calculated density matches that of the recovered  $f(|\mathbf{w}|_{0.875}, \mu)$  distribution. The isotropic solution in Figure 7(a) provides a good match to the measured  $f_{+T}(v)$  values and the higher  $E/q$  steps of the measured  $f_{-T}(v)$  with a normalized (i.e., divided by the number of  $E/q$  steps used) regression residual of 0.22. However, this solution underestimates the  $f_{-T}(v)$  phase-space densities measured at  $E/q < 3 \text{ keV/e}$ . The hemispherical solution in Figure 7(b) provides marginal improvement, with a normalized regression residual of 0.18 and an underestimation of the measured  $f_{-T}(v)$  phase-space densities for  $E/q < 2 \text{ keV/e}$ . Only by further increasing the angular structure of the solution to  $30^\circ$  (Figure 7(c)) or  $15^\circ$  (Figure 7(d)) can we fully reproduce the spacecraft observations. For these cases, the solutions nearly monotonically decrease with pitch angle, with normalized residuals of 0.08 and 0.05 for the  $30^\circ$  and  $15^\circ$  solutions, respectively. From these solutions, our best estimate of  $f(|\mathbf{w}|_{0.875}, \mu)$  resembles a newly injected  $\text{He}^+$  distribution that has not yet pitch-angle scattered to isotropy, consistent with the findings of Oka et al. (2002) and Drews et al. (2013). The density and velocity of the

$\text{He}^+$  in the  $|\mathbf{w}|_{0.875}$  shell using the  $15^\circ$  resolution distribution and for  $|\mathbf{w}| = 0.875$  and  $\Delta|\mathbf{w}| = 0.25$  are  $n_{\text{He}^+} = 0.0033 \pm 0.00030 \text{ cm}^{-3}$  and  $v_{\text{He}^+} = 230 \pm 17 \text{ km s}^{-1}$ .

#### 4.2.2. Recovery of the $|\mathbf{w}|_{0.625}$ Shell

With a known  $f(|\mathbf{w}|_{0.875}, \mu)$  solution, we can solve for  $f(|\mathbf{w}|_{0.625}, \mu)$  using Equation (8) and the lower  $E/q$  steps of the  $+T$  orientation. Here we use the  $15^\circ$   $f(|\mathbf{w}|_{0.875}, \mu)$  distribution. As shown in Figure 8(a), phase-space density in this shell does not bear as strong a resemblance to the modeled injection distribution, though it does appear to decrease with decreasing pitch angle. This behavior is expected of a distribution comprised of older  $\text{He}^+$  ions that has had more time to evolve, though it is important to note that this distribution is less well observed than that of the  $|\mathbf{w}|_{0.875}$  shell. The density and velocity of the  $f(|\mathbf{w}|_{0.625}, \mu)$  shell are  $n_{\text{He}^+} = 0.0027 \pm 0.00039 \text{ cm}^{-3}$  and  $v_{\text{He}^+} = 276 \pm 11 \text{ km s}^{-1}$ .

### 5. ANALYSIS AND DISCUSSION

The recovered distribution function  $f(|\mathbf{w}|, \mu)$  can be used to infer properties about physical processes in the inner heliosphere. Here, we use the density of  $\text{He}^+$  in each  $|\mathbf{w}|$  shell to estimate production rate of neutral helium as a function of heliocentric distance, and we use the angular structure of the



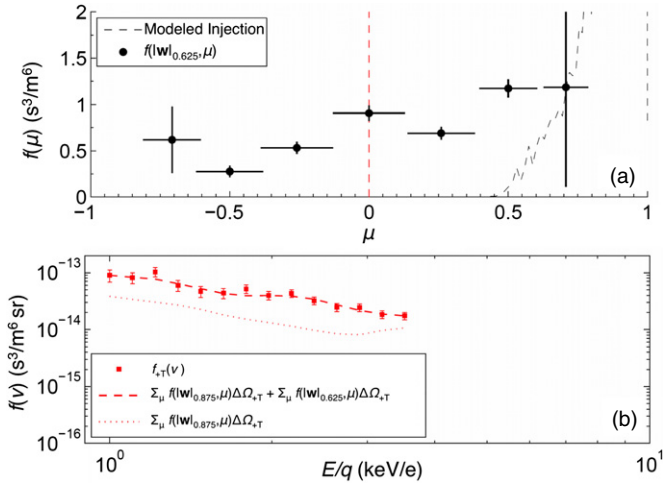


**Figure 8.** (a) Recovered phase-space density as a function of magnetic pitch angle for the  $|w|_{0.625}$  shell for a solution with  $15^\circ$  angular resolution. (b) Measured  $f_{+T}(v)$  values for  $E/q < 3.5$  keV/e. The contribution of the  $|w|_{0.875}$  shell to  $\sum_{|w|, \mu} f(|w|, \mu) \Delta\Omega(|w|, \mu, v)$  is indicated with a dotted red line. The total  $\sum_{|w|, \mu} f(|w|, \mu) \Delta\Omega(|w|, \mu, v)$  values calculated using both  $|w|$  shells are indicated with a dashed red line.

(A color version of this figure is available in the online journal.)

distribution compared with the initial injection to estimate the pitch-angle scattering rate.

### 5.1. Helium Production Rates

Consider the steady-state, spherically symmetric continuity equation of  $\text{He}^+$ . The local production rate of  $\text{He}^+$  is defined here as the product of the neutral helium density ( $n_{\text{He}}$ ) and the ionization rate ( $\beta_{\text{He}}$ ) and will create new helium pickup ions at  $|w| = 1$  according to

$$n_{\text{He}} \beta_{\text{He}} = \nabla \cdot (n_{\text{He}} v_{\text{He}^+}) = \frac{1}{R^2} \frac{\partial}{\partial R} (R^2 n_{\text{He}} v_{\text{He}^+}) \approx \left( \frac{2}{\bar{R}} \right) n_{\text{He}^+}(\bar{R}) v_{\text{He}^+}(\bar{R}), \quad (9)$$

where  $\bar{R}$  is the heliocentric distance of initial ion pickup and we have assumed that the  $\text{He}^+$  distribution varies slowly with  $R$ , i.e.,  $\partial(n_{\text{He}^+} v_{\text{He}^+})/\partial R \ll (n_{\text{He}^+} v_{\text{He}^+}/R)$ , near  $\bar{R}$ . Here we assume that the produced  $\text{He}^+$  distribution is approximately constant over distances  $\bar{R} \pm \Delta R/2$ , after which they are free to evolve with increasing heliocentric distance, and we neglect the non-radial components of  $v_{\text{He}^+}$ . Therefore, measurements of  $n_{\text{He}^+}$  and  $v_{\text{He}^+}$  made on different  $|w|$  shells at heliocentric distance  $R \geq \bar{R}$ , once scaled appropriately, can provide estimates of  $n_{\text{He}^+}(\bar{R})$  and  $v_{\text{He}^+}(\bar{R})$ , which in turn can be used to calculate  $n_{\text{He}} \beta_{\text{He}}$ . These estimates of production rates can then be compared with predictions from neutral models.

With new pickup ions being produced only on the  $|w| = 1$  shell, quasi-radial solar wind IMF expansion and cooling of pickup ions serve to decrease and increase  $n_{\text{He}^+}$  on a given  $|w|$  shell as  $\sim 1/R^2$  and  $\sim R^{2\gamma}$ , respectively. We therefore estimate the value of  $n_{\text{He}^+}(\bar{R})$  by scaling the FIPS-measured  $n_{\text{He}^+}$  value in each shell by  $(0.3 \text{ AU}/\bar{R}^{2(\gamma-1)})$ , where  $\bar{R} = (0.3 \text{ AU})|w|^\gamma$ . Systematic uncertainties in the density of  $\text{He}^+$  could serve to shift the production rates to higher or lower densities. We expect any systematic bias to be constrained to within a factor of  $\sim 2$ . Finally, we take the range of  $v_{\text{He}^+}(\bar{R})$  values to within the initial modeled injection velocity from Section 4.1 and the

FIPS-measured  $v_{\text{He}^+}$  value in each shell. This range of velocities results in a range of production rates for a given  $\gamma$ . For an average cooling index  $\gamma = 1.5$ , we calculate  $n_{\text{He}} \beta_{\text{He}}$  production rates of  $\sim 0.079 \pm 0.057 \text{ m}^{-3} \text{ s}^{-1}$  and  $0.032 \pm 0.019 \text{ m}^{-3} \text{ s}^{-1}$  at  $R \sim 0.15 \text{ AU}$  and  $R \sim 0.25 \text{ AU}$ , respectively.

We then use the Thomas (1978) model to solve for the distribution of neutral helium in the heliosphere under the assumption of spherical symmetry. We also include a component in the model that enables the use of an arbitrary radial dependence of helium ionization rates (Rucinski & Fahr 1989). This model is identical to that used in a previous *MESSENGER* study of  $\text{He}^+$  (Gershman et al. 2013). ISM neutral helium parameters from recent measurements by the *Interstellar Boundary Explorer* (Möbius et al. 2012; Bzowski et al. 2012) were used with  $v_\infty = 23.5 \text{ km s}^{-1}$  and  $T_\infty = 6200 \text{ K}$ , where  $v_\infty$  and  $T_\infty$  are the flow speed and temperature of the neutral interstellar helium, respectively. The density of neutral helium in the ISM was taken to be  $n_\infty = 0.015 \text{ cm}^{-3}$  (Möbius et al. 2004). The heliospheric density,  $n_{\text{He}}$ , was calculated as a function of  $R$  for an average angular distance of  $15^\circ$  from the cone center.

The radial dependence of the helium ionization rate was calculated using a density and temperature of the core and halo electron populations at 1 AU of ( $n_{e-} = 5.37 \text{ cm}^{-3}$ ,  $T_{e-} = 0.135 \text{ MK}$ ) and ( $n_{e-} = 0.22 \text{ cm}^{-3}$ ,  $T_{e-} = 0.63 \text{ MK}$ ), respectively, and a 1 AU photoionization rate of  $5 \times 10^{-8} \text{ s}^{-1}$  (Gershman et al. 2013). The electron temperature was scaled to other heliocentric distances as  $R^{-\alpha}$ , where  $\alpha$  is a constant. However, as McMullin et al. (2004) pointed out, a single temperature scaling will not necessarily provide a complete description of heliospheric electrons inside 1 AU. Here, instead of attempting to match our observations precisely, we generate multiple distributions of heliospheric neutral helium with varying  $\alpha$  to provide a baseline comparison. Helium ionization rates and corresponding neutral densities for photoionization only, with  $\alpha = 0.33$ ,  $\alpha = 0.67$ , and  $\alpha = 1.00$ , are shown in Figures 9(a) and (b), respectively. Increased ionization close to the Sun leads to a decreased neutral helium density inside 0.3 AU.

The  $\text{He}^+$  production rate  $n_{\text{He}} \beta_{\text{He}}$  is shown for the four ionization profiles as a function of radial distance in Figure 9(c). With increasing electron-impact ionization inside  $R = 0.3 \text{ AU}$ , the  $\text{He}^+$  production rate decreases due to the lack of neutral helium available to ionize. The full range of production rates calculated from the  $|w|_{0.625}$  and  $|w|_{0.875}$   $\text{He}^+$  measurements are included in Figure 9(c) for cooling indices between  $\gamma = 1$  and  $\gamma = 2$ . The average measured production rates of  $\sim 0.05 \text{ m}^{-3} \text{ s}^{-1}$  are low compared with the predictions of these simple neutral models. We conclude that even when in deep solar minimum, the Sun creates a cavity nearly devoid of neutral helium inside  $\sim 0.1 \text{ AU}$ .

### 5.2. Pitch-angle Scattering

In a slow solar wind stream in the presence of both Alfvénic and compressive turbulence, particles should be able to efficiently scatter both within and beyond a pitch angle of  $90^\circ$ . To estimate the pitch-angle scattering rate for such a case, we examine a simple one-dimensional diffusion equation with constant diffusion coefficient,  $D_{\mu\mu}$ , and reflective boundary conditions at  $\mu = -1$  and  $\mu = 1$ :

$$\frac{\partial f(\mu, t)}{\partial t} = -D_{\mu\mu} \frac{\partial^2 f(\mu, t)}{\partial^2 \mu}. \quad (10)$$

More comprehensive models of pitch-angle distribution function evolution will include diffusion equations with many

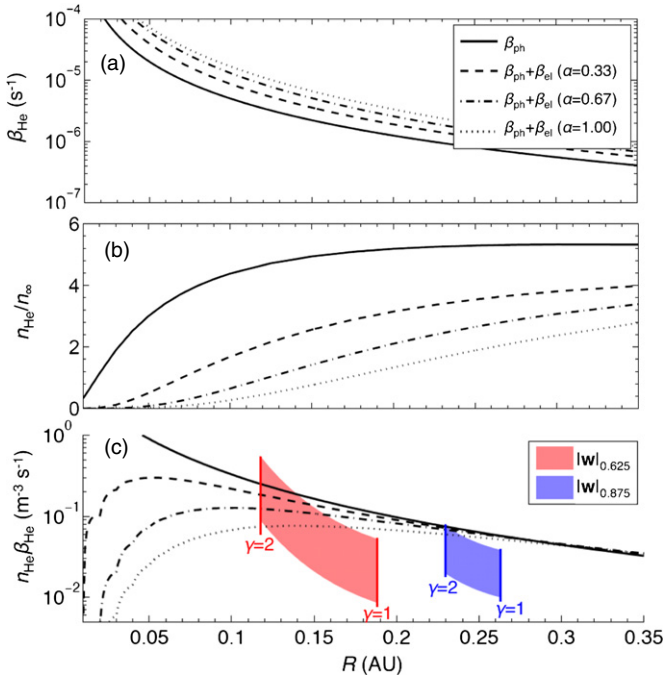


**Figure 9.** (a) Helium ionization rate  $\beta_{\text{He}}$ , (b) neutral helium density,  $n_{\text{He}}$ , and (c)  $\text{He}^+$  production rate  $n_{\text{He}}\beta_{\text{He}}$  as functions of heliocentric distance,  $R$ , for electron temperatures scaling as  $R^{-\alpha}$ .  $\beta_{\text{ph}}$  and  $\beta_{\text{el}}$  refer to the contributions of photoionization and electron-impact ionization to the total  $\beta_{\text{He}}$  value, respectively. The helium production rates calculated from FIPS measurements are included. Increased ionization rates close to the Sun reduce the neutral helium available for conversion into  $\text{He}^+$ . The overestimation of helium density by the models implies that the electron-impact ionization increases rapidly inward of 0.3 AU.

(A color version of this figure is available in the online journal.)

additional terms and allow for angular structure within  $D_{\mu\mu}$  (Chalov & Fahr 1998; Lu & Zank 2001). Although the solution of such equations is beyond the scope of this work, the  $\Delta\Omega$  coefficients and measured  $f(v)$  values are listed in Tables 1–5 in the Appendix. These values can be used to compare predictions of  $f(\mu)$  from more sophisticated models with the  $\text{He}^+$  measurements presented here.

The solution to Equation (10) at time  $\Delta t$  will be a function of an unscattered pitch-angle distribution  $f(\mu, t=0)$  and the quantity  $D_{\mu\mu}\Delta t$ , as shown in Figures 10(a) and (b) for the  $|\mathbf{w}|_{0.875}$  and  $|\mathbf{w}|_{0.625}$  shells, respectively. Here, the initial pitch-angle distributions are those of the modeled ion injections from Section 4.1. As expected, increasing  $D_{\mu\mu}\Delta t$  results in more isotropic pitch-angle distributions. For the  $|\mathbf{w}|_{0.875}$  shell, no value of  $D_{\mu\mu}\Delta t$  appears to match the entire distribution, though the curves for  $D_{\mu\mu}\Delta t$  between 0.05 and 0.15 and  $D_{\mu\mu}\Delta t$  between 0.35 and 0.55 match the  $\mu > 0$  and  $\mu < 0$  distributions well, respectively. We therefore use the average value of  $D_{\mu\mu}\Delta t = 0.35$  to represent the  $|\mathbf{w}|_{0.875}$  shell. For the  $|\mathbf{w}|_{0.625}$  shell, which is more isotropic, the  $D_{\mu\mu}\Delta t = 0.55$  solution matches the entire measured distribution. Given the range of convection velocities and heliocentric distances for the particles in each shell, we estimate that  $D_{\mu\mu} \sim 10^{-6} \text{ s}^{-1}$  for both the  $|\mathbf{w}|_{0.875}$  and  $|\mathbf{w}|_{0.625}$  shells.

The parallel-scattering mean free path,  $\lambda_{\parallel}$  can be calculated from  $D_{\mu\mu}$ , following Hasselmann & Wibberenz (1970) and Isenberg (1997),

$$\lambda_{\parallel} = \frac{3v_{\text{He}^+}}{8} \int_{-1}^1 d\mu \frac{(1-\mu^2)^2}{D_{\mu\mu}}. \quad (11)$$

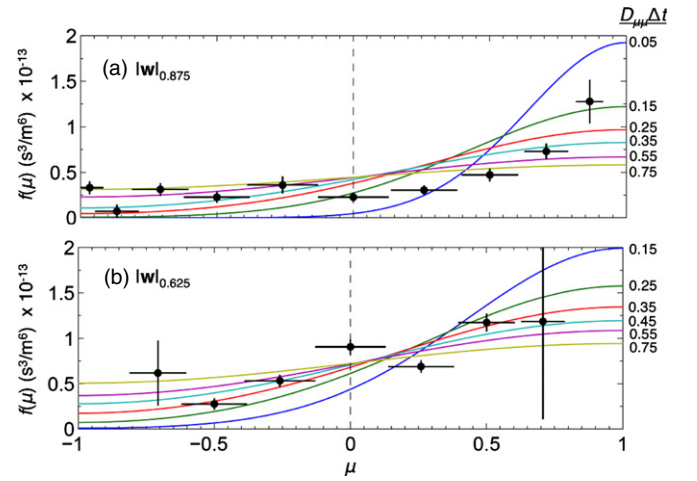


**Figure 10.** Evolution of modeled pitch-angle distribution  $f(\mu)$  for the (a)  $|\mathbf{w}|_{0.875}$  and (b)  $|\mathbf{w}|_{0.625}$  shells. The recovered distributions for each shell are shown as black data points. The injection pitch-angle distributions from Figure 5 were diffused following Equation (10) for various values of  $D_{\mu\mu}\Delta t$ , and the results are shown as solid lines. The  $|\mathbf{w}|_{0.625}$  shell requires a larger  $D_{\mu\mu}\Delta t$  to best match the measured data, consistent with an older pickup-ion distribution.

(A color version of this figure is available in the online journal.)

For a constant  $D_{\mu\mu}$  and  $v_{\text{He}^+}$  approximated by  $\Delta R/\Delta t$ , Equation (11) can be written as

$$\lambda_{\parallel} \approx \frac{2}{5} \frac{R}{D_{\mu\mu}t}. \quad (12)$$

Equation (12) results in an estimated  $\lambda_{\parallel} \sim 0.1 \text{ AU}$  for both the  $|\mathbf{w}|_{0.875}$  and  $|\mathbf{w}|_{0.625}$  shells. This value is of the same order as that calculated from observations by Saul et al. (2007) for the case of high turbulent wave power at 1 AU. Although a large ( $\lambda_{\parallel} \sim 1 \text{ AU}$ ) mean free path may be more commonly observed at 1 AU and beyond, the higher average magnetic fluctuation power in the inner heliosphere likely results in increased average pitch-angle scattering rates. We also note that measurements of large mean paths for pickup ions beyond 1 AU were made over the solar poles (Gloeckler et al. 1995; Gloeckler & Geiss 1998), a characteristically different turbulent environment than those corresponding to these observations.

## 6. CONCLUSIONS

With a new method for the calculation of energy pitch-angle distributions of pickup ions from sectorized  $E/q$  spacecraft measurements from *MESSENGER*/FIPS, we have analyzed the three-dimensional structure of  $\text{He}^+$  in the slow solar wind in the helium focusing cone at  $R = 0.3 \text{ AU}$ . We recovered the angular structure of the  $|\mathbf{w}|_{0.625}$  and  $|\mathbf{w}|_{0.875}$  pickup shells in the solar wind frame. From  $\text{He}^+$  density and convection velocity estimates calculated from these distributions, we find a  $\text{He}^+$  production rate ( $n_{\text{He}}\beta_{\text{He}}$ ) inside 0.3 AU of  $\sim 0.05 \text{ m}^{-3} \text{ s}^{-1}$ , indicative of high electron-impact ionization close to the Sun.

The observed  $|\mathbf{w}|_{0.625}$  and  $|\mathbf{w}|_{0.875}$  distributions closely resemble that of newly injected ions, in agreement with analysis of three-dimensional  $\text{He}^+$  measurements at 1 AU by Oka et al. (2002) and Drews et al. (2013). The distribution of the  $|\mathbf{w}|_{0.625}$  shell is more isotropic than that of the  $|\mathbf{w}|_{0.875}$  shell, consistent with the cooled pickup-ion distribution having had more time to evolve in time and space. For the case studied here, pitch-angle scattering through  $90^\circ$  does not appear to be inhibited with  $\lambda_{\parallel} \sim 0.1 \text{ AU}$ , though a slower overall pitch-angle diffusion coefficient of  $D_{\mu\mu} \sim 10^{-6} \text{ s}^{-1}$  combined with initial ion

**Table 1**  
 $\Delta\Omega$  Coefficients in Units of sr for the  $|\mathbf{w}|_{0.625}$  Shell  
 and the FIPS “–T” Orientation

		Magnetic Pitch Angle (°)			
		30	45	60	75
Energy (keV)	1.00	0.120	0	0	0
	1.10	0.067	0.058	0	0
	1.22	0	0.115	0	0
	1.34	0	0.108	0	0
	1.48	0	0.096	0	0
	1.63	0	0.077	0	0
	1.79	0	0	0.070	0
	1.97	0	0	0.056	0
	2.17	0	0	0.040	0
	2.39	0	0	0.017	0
	2.64	0	0	0	0.012
	2.90	0	0	0	0

**Table 2**  
 $\Delta\Omega$  Coefficients in Units of sr for the  $|\mathbf{w}|_{0.875}$  Shell  
 and the FIPS “–T” Orientation

		Magnetic Pitch Angle (°)				
		30	45	60	75	90
Energy (keV)	1.00	0.448	0.081	0	0	0
	1.10	0.313	0.182	0	0	0
	1.22	0.129	0.336	0	0	0
	1.34	0.019	0.412	0	0	0
	1.48	0	0.403	0	0	0
	1.63	0	0.370	0	0	0
	1.79	0	0.269	0.084	0	0
	1.97	0	0.106	0.221	0	0
	2.17	0	0.010	0.290	0	0
	2.39	0	0	0.269	0	0
	2.64	0	0	0.178	0.061	0
	2.90	0	0	0.063	0.140	0
	3.20	0	0	0	0.160	0
	3.52	0	0	0	0.107	0
	3.88	0	0	0	0.038	0.032
	4.27	0	0	0	0	0.033
	4.70	0	0	0	0	0

gyration confined to  $v < v_{sw}$  in the instrument frame naturally produces a sunward/anti-sunward anisotropy in a quasi-radially oriented IMF.

Measurements of pickup  $\text{He}^+$  inside Earth’s orbit provide an opportunity to analyze a near-pristine pickup-ion distribution having a structure that is primarily a function of particle injection, pitch-angle scattering, and cooling processes. Compared with those observed at 1 AU, these distributions are substantially more sensitive to the electron-impact ionization rates close to the Sun, making their modeling both challenging and elucidating. Currently in orbit around Mercury in its extended mission operations, *MESSENGER* continuously measures  $\text{He}^+$  around Mercury’s space environment between 0.31 and 0.47 AU. The upcoming Solar Orbiter mission will have an orbit that traverses a similar range of heliocentric distances with an instrument complement specifically designed to measure heavy solar wind species and pickup ions (Marsch et al. 2005). Such observations will markedly improve our understanding of the radial evolution of the pickup process.

The *MESSENGER* project is supported by the NASA Discovery Program under contracts NAS5-97271 to The Johns Hopkins University Applied Physics Laboratory and NASW-00002 to the Carnegie Institution of Washington. D.J.G. is supported by an appointment to the NASA Postdoctoral Program at Goddard Space Flight Center, administered by Oak Ridge Associated Universities.

## APPENDIX

### FIPS FIELD OF VIEW COEFFICIENTS

To aid future modeling efforts, the  $\Delta\Omega$  coefficients for each  $|\mathbf{w}|$  shell from Figure 5 are included here in Tables 1–4 as a function of magnetic pitch-angle bin center and FIPS energy step. For bins that are not included in the tables, the coefficients should be considered to be zero. These coefficients can be used in conjunction with predicted  $f(|\mathbf{w}|, \mu)$  values in units of  $\text{s}^6 \text{m}^{-3}$  to predict instrument  $f_{-T}(v)$  and  $f_{+T}(v)$  distributions in units of  $\text{s}^3 \text{m}^{-6} \text{sr}$  following Section 3. The

**Table 3**  
 $\Delta\Omega$  Coefficients in Units of sr for the  $|\mathbf{w}|_{0.625}$  Shell and the FIPS “+T” Orientation

		Magnetic Pitch Angle (°)								
		45	60	75	90	105	120	135	150	165
Energy (keV)	1.00	0.067	0.372	0	0	0	0	0	0	0
	1.10	0	0.419	0	0	0	0	0	0	0
	1.22	0	0.401	0	0	0	0	0	0	0
	1.34	0	0.223	0.161	0	0	0	0	0	0
	1.48	0	0.091	0.277	0	0	0	0	0	0
	1.63	0	0.012	0.343	0	0	0	0	0	0
	1.79	0	0	0.296	0.042	0	0	0	0	0
	1.97	0	0	0.131	0.193	0	0	0	0	0
	2.17	0	0	0.036	0.275	0	0	0	0	0
	2.39	0	0	0	0.237	0.057	0	0	0	0
	2.64	0	0	0	0.108	0.171	0	0	0	0
	2.90	0	0	0	0.020	0.205	0.031	0	0	0
	3.20	0	0	0	0	0.123	0.096	0	0	0
	3.52	0	0	0	0	0.028	0.132	0.027	0	0
	3.88	0	0	0	0	0	0.084	0.048	0.021	0
	4.27	0	0	0	0	0	0.010	0.058	0.027	0
	4.70	0	0	0	0	0	0	0.014	0.030	0.011
	5.18	0	0	0	0	0	0	0	0.010	0.014



**Table 4**  
 $\Delta\Omega$  Coefficients in Units of sr for the  $|w|_{0.875}$  Shell for the FIPS “+T” Orientation

		Magnetic Pitch Angle (°)										
		30	45	60	75	90	105	120	135	150	165	180
	1.00	0	0.257	0.419	0	0	0	0	0	0	0	0
	1.10	0	0.165	0.467	0	0	0	0	0	0	0	0
	1.22	0	0.104	0.486	0	0	0	0	0	0	0	0
	1.34	0	0.058	0.473	0.016	0	0	0	0	0	0	0
	1.48	0	0.024	0.37	0.117	0	0	0	0	0	0	0
	1.63	0	0	0.228	0.243	0	0	0	0	0	0	0
	1.79	0	0	0.109	0.334	0	0	0	0	0	0	0
	1.97	0	0	0.045	0.368	0	0	0	0	0	0	0
	2.17	0	0	0.013	0.308	0.067	0	0	0	0	0	0
	2.39	0	0	0	0.186	0.18	0	0	0	0	0	0
Energy (keV)	2.64	0	0	0	0.066	0.285	0	0	0	0	0	0
	2.90	0	0	0	0	0.286	0.046	0	0	0	0	0
	3.20	0	0	0	0	0.182	0.154	0	0	0	0	0
	3.52	0	0	0	0	0.07	0.254	0	0	0	0	0
	3.88	0	0	0	0	0	0.224	0.091	0	0	0	0
	4.27	0	0	0	0	0	0.108	0.193	0	0	0	0
	4.70	0	0	0	0	0	0.017	0.185	0.077	0	0	0
	5.18	0	0	0	0	0	0	0.083	0.114	0.024	0	0
	5.70	0	0	0	0	0	0	0.004	0.099	0.037	0.018	0
	6.28	0	0	0	0	0	0	0	0.011	0.042	0.021	0
	6.91	0	0	0	0	0	0	0	0	0	0.023	0

**Table 5**  
 FIPS-measured  $f(v)$  Distributions for the “−T” and “+T” Orientations

Energy (keV)	$f_{-T}(v)$ ( $10^{-13} \text{ s}^3 \text{ m}^{-6} \text{ sr}$ )	$f_{+T}(v)$ ( $10^{-13} \text{ s}^3 \text{ m}^{-6} \text{ sr}$ )
1.00	$0.621 \pm 0.187$	$1.023 \pm 0.241$
1.10	$0.738 \pm 0.185$	$0.939 \pm 0.210$
1.22	$0.528 \pm 0.141$	$1.178 \pm 0.212$
1.34	$0.431 \pm 0.115$	$0.683 \pm 0.146$
1.48	$0.403 \pm 0.101$	$0.533 \pm 0.116$
1.63	$0.226 \pm 0.068$	$0.497 \pm 0.101$
1.79	$0.285 \pm 0.069$	$0.592 \pm 0.100$
1.97	$0.315 \pm 0.066$	$0.455 \pm 0.079$
2.17	$0.245 \pm 0.052$	$0.494 \pm 0.074$
2.39	$0.154 \pm 0.037$	$0.366 \pm 0.058$
2.64	$0.103 \pm 0.028$	$0.283 \pm 0.046$
2.90	$0.054 \pm 0.018$	$0.278 \pm 0.041$
3.20	$0.083 \pm 0.020$	$0.211 \pm 0.032$
3.52	$0.043 \pm 0.013$	$0.199 \pm 0.028$
3.88	$0.032 \pm 0.010$	$0.109 \pm 0.019$
4.27	$0.008 \pm 0.005$	$0.109 \pm 0.017$
4.70	$0.004 \pm 0.003$	$0.071 \pm 0.012$
5.18	$0.002 \pm 0.002$	$0.076 \pm 0.011$
5.70	$0.000 \pm 0.000$	$0.043 \pm 0.008$
6.28	$0.0001 \pm 0.0001$	$0.015 \pm 0.004$
6.91	$0.000 \pm 0.000$	$0.009 \pm 0.003$

relevant instrument-measured  $f_{+T}(v)$  and  $f_{-T}(v)$  distributions are included in Table 5 to be used as a comparison with model predictions. The uncertainties here are from counting errors and do not reflect any systematic uncertainties that may be present in the instrument data. However, we estimate systematic uncertainties to be constrained to within a factor of two.

## REFERENCES

Anderson, B. J., Acuña, M. H., Lohr, D. A., et al. 2007, *SSRv*, **131**, 417  
 Andrews, G. B., Zurbuchen, T. H., Mauk, B. H., et al. 2007, *SSRv*, **131**, 523  
 Bavassano, B., Dobrowolny, M., Mariani, F., & Ness, N. F. 1982, *JGR*, **87**, 3617  
 Bavassano, B., & Smith, E. J. 1986, *JGR*, **91**, 1706

Belcher, J. W., & Davis, L., Jr. 1971, *JGR*, **76**, 3534  
 Blum, P. W., & Fahr, H. J. 1970, *A&A*, **4**, 280  
 Bzowski, M., Kubiak, M. A., Möbius, E., et al. 2012, *ApJS*, **198**, 12  
 Chalov, S. V., & Fahr, H. J. 1998, *A&A*, **335**, 746  
 Chalov, S. V., & Fahr, H. J. 2000, *A&A*, **360**, 381  
 Chen, J. H., Möbius, E., Gloeckler, G., et al. 2013, *JGR*, **118**, 3946  
 Drews, C., Berger, L., Wimmer-Schweingruber, R. F., et al. 2012, *JGR*, **117**, A09106  
 Drews, C., Berger, L., Wimmer-Schweingruber, R. F., & Galvin, A. B. 2013, *GeoRL*, **40**, 1468  
 Fahr, H. J. 1968, *Ap&SS*, **2**, 474  
 Fahr, H. J. 1971, *A&A*, **14**, 263  
 Fisk, L. A., & Gloeckler, G. 2012, *SSRv*, **173**, 433  
 Fisk, L. A., Schwadron, N. A., & Gloeckler, G. 1997, *GeoRL*, **24**, 93  
 Fraser, B. J. 1985, *SSRv*, **42**, 357  
 Gershman, D. J., Gloeckler, G., Gilbert, J. A., et al. 2013, *JGRA*, **118**, 1389  
 Gershman, D. J., Zurbuchen, T. H., Fisk, L. A., et al. 2012, *JGR*, **117**, A00M02  
 Gilbert, J. A., Lepri, S. T., Landi, E., & Zurbuchen, T. H. 2012, *ApJ*, **751**, 20  
 Gloeckler, G., & Geiss, J. 1998, *SSRv*, **86**, 127  
 Gloeckler, G., & Geiss, J. 2001, *SSRv*, **97**, 169  
 Gloeckler, G., Möbius, E., & Geiss, J. 2004, *A&A*, **426**, 845  
 Gloeckler, G., Schwadron, N. A., Fisk, L. A., & Geiss, J. 1995, *GeoRL*, **22**, 2665  
 Gosling, J. T., McComas, D. J., Roberts, D. A., & Skoug, R. M. 2009, *ApJL*, **695**, L213  
 Hasselmann, K., & Wibberenz, G. 1970, *ApJ*, **162**, 1049  
 Huddleston, D. E., Strangeway, R. J., Warnecke, J., Russell, C. T., & Kivelson, M. G. 1998, *JGR*, **103**, 19887  
 Isenberg, P. A. 1987, *JGR*, **92**, 8795  
 Isenberg, P. A. 1997, *JGR*, **102**, 4719  
 Isenberg, P. A., & Vasquez, B. J. 2007, *ApJ*, **668**, 546  
 Issautier, K., Meyer-Vernet, N., Moncuquet, M., & Hoang, S. 1998, *JGR*, **103**, 1969  
 Jian, L. K., Russell, C. T., Luhmann, J. G., et al. 2009, *ApJL*, **701**, L105  
 Jian, L. K., Russell, C. T., Luhmann, J. G., et al. 2010, *JGR*, **115**, A12115  
 Koutroumpa, D., Collier, M. R., Kuntz, K. D., Lallement, R., & Snowden, S. L. 2009, *ApJ*, **697**, 1214  
 Lallement, R., Raymond, J. C., Bertaux, J., et al. 2004, *A&A*, **426**, 867  
 Leisner, J. S., Russell, C. T., Dougherty, M. K., et al. 2006, *GeoRL*, **33**, L11101  
 Lu, J. Y., & Zank, G. P. 2001, *JGR*, **106**, 5709  
 Maksimovic, M., Gary, S. P., & Skoug, R. M. 2000, *JGR*, **105**, 18337  
 Maksimovic, M., Zouganelis, I., Chaufray, J.-Y., et al. 2005, *JGR*, **110**, A09104  
 Marsch, E., Goertz, C. K., & Richter, K. 1982, *JGR*, **87**, 5030  
 Marsch, E., & Tu, C.-Y. 1990, *JGR*, **95**, 8211

- Marsch, E., Marsden, R., Harrison, R., Wimmer-Schweingruber, R., & Fleck, B. 2005, [AdSpR](#), **36**, 1360
- McComas, D. J., Schwadron, N. A., Crary, F. J., et al. 2004, [JGR](#), **109**, A02104
- McMullin, D. R., Bzowski, M., Möbius, E., et al. 2004, [A&A](#), **426**, 885
- Möbius, E. 1996, [SSRv](#), **1**, 375
- Möbius, E., Boschler, P., Bzowski, M., et al. 2012, [ApJS](#), **198**, 11
- Möbius, E., Bzowski, M., Chalov, S., et al. 2004, [A&A](#), **426**, 897
- Möbius, E., Litvinenko, Y., Grüwaldt, H., et al. 1999, [GeoRL](#), **26**, 3181
- Möbius, E., Rucinski, D., Hovestadt, D., & Klecker, B. 1995, [A&A](#), **304**, 505
- Möbius, E., Rucinski, D., Lee, M. A., & Isenberg, P. A. 1998, [JGR](#), **103**, 257
- Neubauer, F. M., Glassmeier, K.-H., Coates, A. J., & Johnstone, A. D. 1993, [JGR](#), **98**, 20937
- Noda, H., Terasawa, T., Saito, Y., et al. 2001, [SSRv](#), **97**, 423
- Oka, M., Terasawa, T., Noda, H., Saito, Y., & Mukai, T. 2002, [GeoRL](#), **29**, 54-1
- Pilipp, W. G., Miggenrieder, H., Mühlhäuser, K.-H., et al. 1987, [JGR](#), **92**, 1103
- Raines, J. M., Slavin, J. A., Zurbuchen, T. H., et al. 2011, [P&SS](#), **59**, 2004
- Rucinski, D., & Fahr, H. J. 1989, [A&A](#), **224**, 290
- Samson, J. A. R., He, Z. X., Yin, L., & Haddad, G. N. 1994, [JPhB](#), **27**, 887
- Saul, L., Möbius, E., Isenberg, P. A., & Bochsler, P. 2007, [ApJ](#), **655**, 672
- Saul, L., Möbius, E., & Smith, C. W. 2004, in AIP Conf. Proc. 719, Physics of the Outer Heliosphere, ed. V. Florinski et al. (Melville, NY: AIP), 207
- Saul, L., Wurz, P., & Kallenbach, R. 2009, [ApJ](#), **703**, 325
- Schlickeiser, R. 1989, [ApJ](#), **336**, 243
- Schwadron, N. A. 1998, [JGR](#), **103**, 20643
- Solomon, S. C., McNutt, R. L., Jr., Gold, R. E., et al. 2001, [P&SS](#), **49**, 1445
- Thomas, G. E. 1978, [AREPS](#), **6**, 173
- Tu, C.-Y., & Marsch, E. 1995, [SSRv](#), **73**, 1
- Vallerga, J., Lallement, R., Lemoine, M., Dalaudier, F., & McMullin, D. 2004, [A&A](#), **426**, 855
- Vasyliunas, V. M., & Siscoe, G. L. 1976, [JGR](#), **81**, 1247
- Witte, M., Banaszkiewicz, M., Rosenbauer, H., & McMullin, D. 2004, [AdSpR](#), **34**, 61
- Witte, M., Rosenbauer, H., Banaszkiewicz, M., & Fahr, H. 1993, [AdSpR](#), **13**, 121